

# BENCHMARK SOLUTIONS OF SOME STRUCTURAL ANALYSIS PROBLEMS USING FINITE-VOLUME METHOD AND MULTIGRID ACCELERATION

I. DEMIRDŽIĆ

*Mašinski fakultet, Omladinsko šetalište bb, 71000 Sarajevo, Bosnia and Herzegovina*

S. MUZAFERLIJA\* AND M. PERIĆ

*Institut für Schiffbau, Universität Hamburg, Lämmersieth 90, D-22305 Hamburg, Germany*

## SUMMARY

In this paper a set of benchmark test cases for solid-body stress analysis and their solutions are presented. The results are obtained using finite-volume discretization and segregated solution procedure. Sets of progressively finer grids are used in a full multigrid algorithm based on V cycles and a correction scheme, ensuring high computational efficiency. Solutions obtained on systematically refined grids are used to estimate the solution error, which was found to be less than 1 per cent on the finest grids. In addition to graphical presentation of the solutions, tabular data for some characteristic profiles is included to make future comparisons easier. Some details about the convergence properties of the method as well as an outline of the methodology are also presented. It is hoped that the test problems and the solutions presented in this paper will be used in the future for assessing the accuracy and efficiency of new solution methods for solid-body stress analysis. © 1997 by John Wiley & Sons, Ltd.

KEY WORDS: finite-volume stress analysis; multigrid

## 1. INTRODUCTION

For the development of a new solution method or for the validation of an existing one, it is important to have a set of test cases with accurate solutions for comparison purposes. Most test cases available in literature lack systematic grid-dependence tests. Sometimes they were not possible, since finite element (FE) methods and block solvers were used, so that successive and uniform grid refinement would demand resources which were not available. The efficiency of the algorithm and its execution time can also discourage one from performing such tests.

The finite-volume (FV) methods based on a segregated approach<sup>1,2</sup> are very efficient in terms of computer memory. Once these methods are equipped with a multigrid accelerator of outer iterations,<sup>3</sup> they become extremely efficient regarding computing time as well. These two techniques are described and used in this paper to obtain efficiently accurate solutions suitable for benchmarking.

---

\*On leave from the Faculty of Mechanical Engineering, University of Sarajevo, Bosnia and Herzegovina

In Section 2 the mathematical model of solid-body equilibrium is presented. In Section 3 the FV discretization procedure and an algorithm for an iterative solution of the resulting algebraic equations are briefly described. The results for selected cases are presented in Section 4.

## 2. GOVERNING EQUATIONS

The mathematical model of elastic solid-body equilibrium, consisting of the momentum equation in integral form, Hooke's law and boundary conditions, serves as a starting point for the FV discretization method used in this study. In this case the static equilibrium of an arbitrary part of solid body of volume  $V$  bounded by a surface  $S$  can be described by

$$\int_S \{ \mu [\text{grad } \mathbf{u} + (\text{grad } \mathbf{u})^T] + \lambda \text{div } \mathbf{u} \mathbf{I} \} \cdot \mathbf{ds} + \int_V \mathbf{f} dV = 0 \quad (1)$$

where  $\mathbf{u}$  is the displacement vector,  $\mu$  and  $\lambda$  are Lamé's coefficients,  $\mathbf{I}$  the unit tensor,  $\mathbf{ds}$  is the outward-pointing surface-element vector and  $\mathbf{f}$  is the resultant body force.

The problem is of an elliptic nature, so boundary conditions have to be specified at all solution domain boundaries. They can be of Dirichlet type (*displacement boundary conditions*):

$$\mathbf{u}(\mathbf{r}) = \mathbf{u}_B, \quad \mathbf{r} \in S_D \quad (2)$$

or of Neumann type (*traction boundary conditions*):

$$\boldsymbol{\sigma}(\mathbf{r}) \cdot \mathbf{n}(\mathbf{r}) = \mathbf{t}_B, \quad \mathbf{r} \in S_T \quad (3)$$

where  $\mathbf{r}$  is the position vector,  $\mathbf{n}$  the unit vector normal to the boundary surface and  $\mathbf{u}_B$  and  $\mathbf{t}_B$  are the prescribed boundary displacement and surface traction, respectively.  $S_D$  and  $S_T$  are parts of the boundary on which Dirichlet and Neumann boundary conditions apply, respectively.

In some cases symmetry conditions will be used to reduce the problem size.

## 3. SOLUTION METHODOLOGY

Full details of the FV technique employed to discretize equation (1) using displacement vector components as unknowns are given in References 1 and 2 so only a brief outline will be presented in this section.

In order to obtain discrete counterparts of equation (1), the solution domain is subdivided into an arbitrary number of contiguous control volumes (CVs) or cells. The computational nodes are placed at their centres, where the value of the displacement vector is stored. The control volume is defined by the co-ordinates of its vertices and it can be of an arbitrary polyhedral shape. No distinction is made between the co-ordinates of vertices before and after deformation, since the displacements are assumed to be relatively small.

Assuming linear spatial distributions of the displacement vector and using the midpoint rule to approximate surface and volume integrals, equation (1) is integrated over each CV to deliver an algebraic equation in which displacement components at cell centres appear as unknowns. The adopted approximations are second-order-accurate.

In order to simplify the solution procedure and to reduce the computer memory necessary for solving the problem, the equations for displacement vector components are decoupled, resulting in a system of linear algebraic equations of the form

$$A\boldsymbol{\phi} = \mathbf{b} \quad (4)$$

for each displacement vector component, where  $A$  is a symmetric sparse  $N \times N$  matrix ( $N$  is the total number of CVs) and the vector  $\boldsymbol{\phi}$  contains values of displacement vector component  $u_i$  at  $N$  nodes. Matrix  $A$  involves only contributions from nearest-neighbour CVs. Contributions from further CVs and from other displacement components are relegated to the right-hand side.

The iterative CGSTAB solver<sup>4</sup> with incomplete Cholesky preconditioning,<sup>5</sup> which retains the sparsity of the original coefficient matrix  $A$ , is used to solve system (4). Iterations within the CGSTAB solver are called *inner iterations*. There is no need to solve system (4) to a tight tolerance since vector  $\mathbf{b}$  is only an approximation (based on the solution from the previous iteration). Normally, reduction of residuals by an order of magnitude suffices. This is usually achieved in 2 to 3 inner iterations.

After equation (4) is solved for all three displacement vector components, vector  $\mathbf{b}$  is updated using the new solution estimate, and the procedure is repeated until a converged solution is obtained. This cycle represents an *outer iteration* of the solution algorithm.

The procedure is assumed converged when the sum of normalized absolute residuals for each displacement vector component has fallen a prescribed number of orders of magnitude (typically four). In order to promote stability of the solution method, underrelaxation is used; typical underrelaxation factors are 0.9–0.95.

The solution procedure described above does not take advantage of the fact that the algebraic system to be solved is actually an approximation to continuous equations, and therefore can be similarly approximated by other much simpler algebraic systems. This fact can be exploited using a multigrid (MG) method,<sup>6</sup> which solves iteratively a system of discretized equations on a given grid by interacting with a hierarchy of coarser grids. In the present study, progressively finer grids are obtained by systematically refining coarse-grid CVs (*parents*) into a number of finer ones (*children*), e.g. a hexahedral CV is subdivided into eight finer hexahedra.

After several outer iterations are performed on a fine grid, the intermediate solution vector  $\boldsymbol{\phi}_f^*$  satisfies equation (4) up to the residual  $\boldsymbol{\rho}_f$ :

$$A_f \boldsymbol{\phi}_f^* = \mathbf{b}_f + \boldsymbol{\rho}_f \quad (5)$$

This equation can be rewritten in terms of corrections on the fine grid,  $\boldsymbol{\delta}_f = \boldsymbol{\phi}_f - \boldsymbol{\phi}_f^*$ , where  $\boldsymbol{\phi}_f$  is the exact solution, as follows:

$$A_f \boldsymbol{\delta}_f = \boldsymbol{\rho}_f \quad (6)$$

Equation (6) has the same structure as equation (4) and represents the transport of the corrections  $\boldsymbol{\delta}_f$  driven by the field of residuals on the fine grid  $\boldsymbol{\rho}_f$ . A similar system of algebraic equations to the one given by equation (6) can be constructed on the coarse grid:

$$A_c \boldsymbol{\delta}_c = \mathbf{b}_c + \boldsymbol{\rho}_c^f \quad (7)$$

where  $A_c$  and  $\mathbf{b}_c$  are calculated on the coarse grid in the same way as their counterparts  $A_f$  and  $\mathbf{b}_f$  are constructed on the fine grid and  $\boldsymbol{\rho}_c^f$  is the fine-grid residual  $\boldsymbol{\rho}_f$  restricted to the coarse grid. The conservation principle requires that  $\boldsymbol{\rho}_c^f$  for each parent cell is obtained by summation of residuals of all its children cells.

The correction  $\boldsymbol{\delta}_c$  that satisfies equation (7) is linearly interpolated (prolongated) to the fine grid and added to the fine-grid solution vector. Since the updated solution on the fine grid will still not, in general, be converged, it is necessary to repeat this two-level cycle until the full convergence is achieved.

When the converged solution on the fine grid is obtained, it is interpolated to the next finer grid to be used as an initial solution. This step is the main difference between MG and the so-called

'full multigrid' (FMG) approach. The multigrid cycle is restarted, but now with two coarser grids. Equation (7) has the same form as (4) ( $\rho_c^f$  can be lumped into  $\mathbf{b}_c$ ), and may itself be solved using a coarser grid, so that the extension of the solution procedure from a two-grid to an arbitrary multigrid scheme is straightforward.

In the present study, only two outer iterations were performed on the fine grid, while on coarser grids four iterations were performed during the restriction and three iterations during the prolongation phase. On the coarsest grid, 30 outer iterations were performed. For a fixed MG cycle these parameters could be optimized for each individual case. However, in the present study the same set was used in all cases.

#### 4. RESULTS

The geometrical flexibility and accuracy of the present method is demonstrated in earlier publications.<sup>1,2,9</sup> In this section very accurate solutions of three representative test cases, chosen as suitable for benchmarking, are presented. The first case is two-dimensional with an analytical solution, allowing direct evaluation of discretization error. The other two cases are three-dimensional problems with relatively simple geometry, but still requiring fine grids to obtain accurate solutions. Since analytical solutions are not available, errors are estimated using Richardson extrapolation. The discretization method is of second order, so the solution error on the finest grid can be estimated as

$$\varepsilon = \frac{\phi_f - \phi_c}{3} \quad (8)$$

where  $\phi_f$  is the solution on the finest and  $\phi_c$  on the next coarser grid.

##### 4.1. Flat plate with a circular hole subjected to a uniform tension

A plate with a circular hole in its centre is loaded by a uniform tension in one direction; cf. Figure 1. If the radius of the hole is small compared to plate dimensions, then an analytical solution, obtained for an infinitely large plate, describes accurately the stress distribution<sup>7,8</sup>

$$\sigma_{xx} = t_x \left[ 1 - \frac{a^2}{r^2} \left( \frac{3}{2} \cos 2\theta + \cos 4\theta \right) + \frac{3}{2} \frac{a^4}{r^4} \cos 4\theta \right]$$

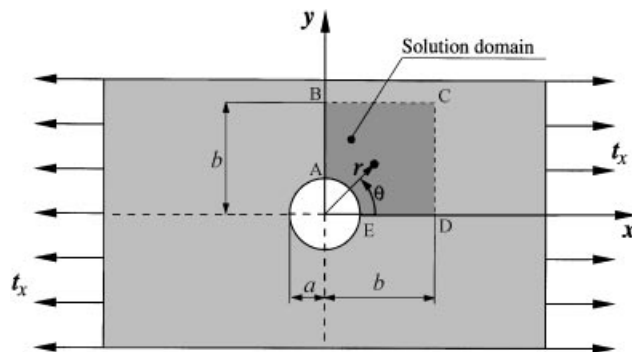


Figure 1. Plate with a central circular hole subjected to unidirectional tensile loads ( $a = 0.5$  m,  $b = 2$  m,  $t_x = 10000$  Pa,  $E = 10^7$  Pa,  $\nu = 0.3$ )

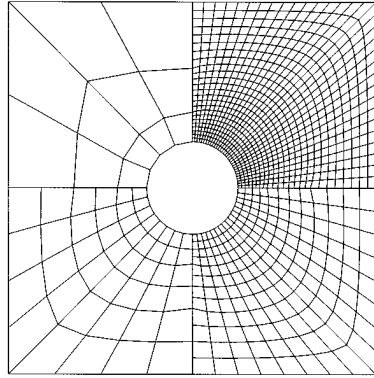


Figure 2. First four numerical grids used for predictions

$$\sigma_{yy} = t_x \left[ -\frac{a^2}{r^2} \left( \frac{1}{2} \cos 2\theta - \cos 4\theta \right) - \frac{3}{2} \frac{a^4}{r^4} \cos 4\theta \right] \quad (9)$$

$$\sigma_{xy} = t_x \left[ -\frac{a^2}{r^2} \left( \frac{1}{2} \sin 2\theta + \sin 4\theta \right) + \frac{3}{2} \frac{a^4}{r^4} \sin 4\theta \right]$$

where  $r = \sqrt{x^2 + y^2}$  and  $\theta = \tan^{-1}(y/x)$  are the usual polar co-ordinates.

Taking into account the symmetry of the problem, the solution domain shown in Figure 1 is used for numerical analysis. In order to eliminate the influence of the finite-plate dimensions, the traction calculated from the analytical solution is imposed at the boundaries BC and CD. At the hole boundary AE, zero traction is specified, and at boundaries AB and DE, symmetry boundary conditions are applied.

The grid-dependence tests are performed by employing six systematically refined grids, four of which are shown in Figure 2. The coarsest grid has 12 while the finest has 12 288 CVs. It is obvious that the finer grids are too fine in the region far from the hole, and by means of local grid refinement a solution of the same accuracy can be obtained with considerably less computational points.<sup>1</sup> However, we look here for grid-independent solutions obtained by systematic grid refinement throughout the computational domain, such that Richardson extrapolation can be used for error estimation without any additional assumptions.

The effect of grid refinement is shown in Figure 3, where the average errors in stresses  $\sigma_{xx}$ ,  $\sigma_{yy}$  and  $\sigma_{xy}$  are plotted as a function of the characteristic grid size. The average is found by summing the weighted absolute values of differences between the predicted stresses and those given by equations (9). The weighting factors are calculated as the ratio of the CV volume and the total volume of the computational domain. The error is normalized with the average value of the corresponding stress in the computational domain. A characteristic grid size is obtained by dividing the square root of the total area of the computational domain in the  $x$ - $y$  plane by the total number of control volumes. Figure 3 shows that the convergence towards the analytical solution is asymptotically of second-order (the error is reducing by a factor of four as the grid is refined). The errors on the finest grid are lower than 0.4 per cent.

The use of the full-multigrid acceleration technique, as can be seen from Figure 4 and Table I, leads to an almost ideal convergence behaviour, since the asymptotic convergence rate is almost

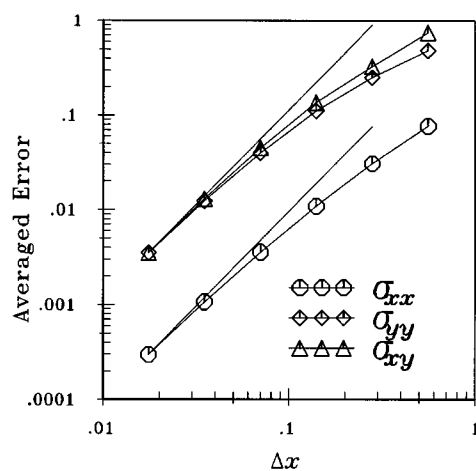


Figure 3. Solution error as a function of the grid size for the plate with circular hole problem (straight lines show ideal slope for a second-order scheme)

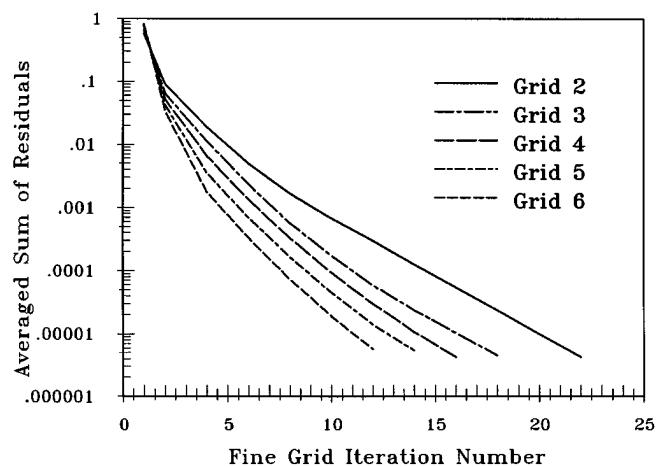


Figure 4. Convergence history of the solution method for the plate with circular hole

Table I. Number of fine grid iterations and computing time necessary to obtain converged results for plate with circular hole problem

Grid no.	No. CV	Iter.	CPU (s)
1	12	43	0.12
2	48	22	0.63
3	192	18	1.78
4	768	16	6.37
5	3072	14	22.87
6	12288	12	78.84

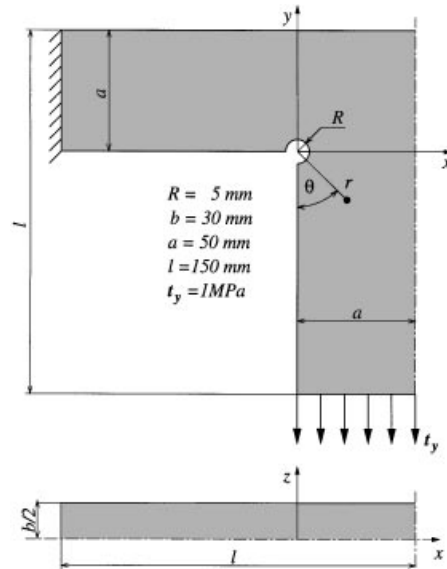


Figure 5. T-profile subjected to unidirectional tensile loads

the same on each grid. Actually, the total number of fine grid iterations reduces as the grid gets finer, due to the effect of using a good initial field provided by the full multigrid.

This test case is suitable for assessing the accuracy and the order of the solution method, since the discretization error can be exactly calculated. Note that two methods of the same order may, on a given grid, have discretization errors which differ by as much as an order of magnitude; the order of the discretization only defines the rate of error reduction with grid refinement and is not a sufficient measure of the method accuracy.

#### 4.2. A narrow member with a T cross-section subjected to a uniform tension

A narrow member with a T cross-section is a common element in engineering and at the same time it has a simple geometry which is easy to define. Holes of radius  $R$  are usually drilled at the otherwise sharp corners in order to reduce stress concentrations. Due to the symmetry of the problem only a quarter of the member has been considered. The solution domain showing dimensions and the prescribed boundary conditions is depicted in Figure 5. The flange is fixed at its two ends while the uniformly distributed traction force acts along the bottom part of the web.

The calculation is performed on four successively refined grids, the coarsest having 624 and the finest 319488 CVs. These two grids are shown in Figure 6 together with the perspective view on the second grid from which one can see the grid distribution in the  $z$  direction.

The distributions of  $\sigma_{xx}$  and  $\sigma_{yy}$  stresses in the  $z = 0$  plane obtained on the finest grid are shown in Figure 7, where one can see the large stress concentration around the hole. Apart from regions around the hole and the fixed end of the member, the distribution of stresses is fairly smooth.

In order to simplify the presentation of the results, profiles of the effective stress, which combines all six independent stress components,

$$\sigma_{\text{eff}} = \sqrt{\frac{1}{2} [(\sigma_{xx} - \sigma_{yy})^2 + (\sigma_{yy} - \sigma_{zz})^2 + (\sigma_{zz} - \sigma_{xx})^2] + 3(\sigma_{xy}^2 + \sigma_{yz}^2 + \sigma_{zx}^2)} \quad (10)$$

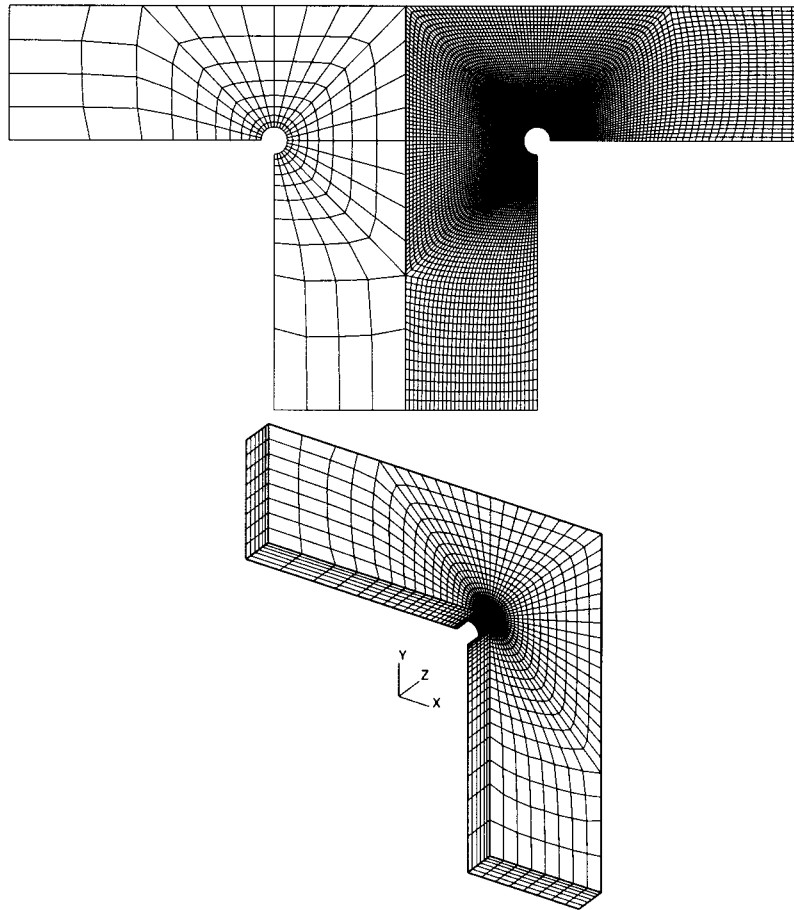


Figure 6. Coarsest and finest numerical grid (top) and perspective view on the second grid (bottom)

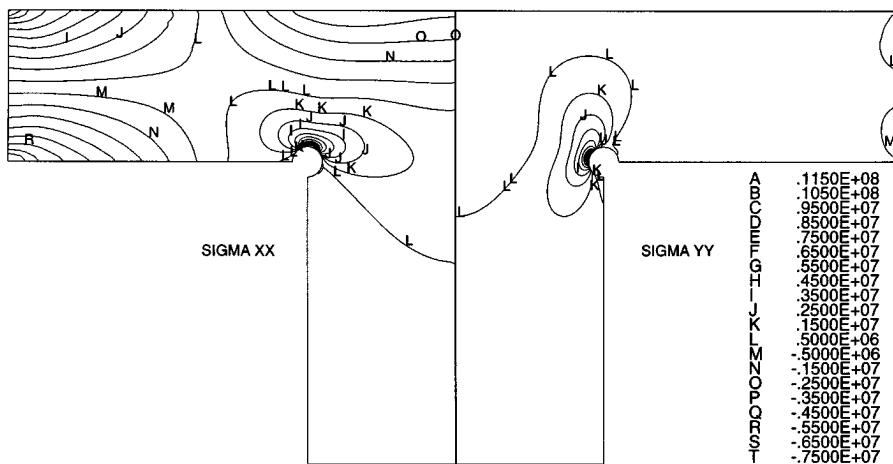


Figure 7. Distribution of  $\sigma_{xx}$  (left) and  $\sigma_{yy}$  (right) stresses in plane  $z = 0$

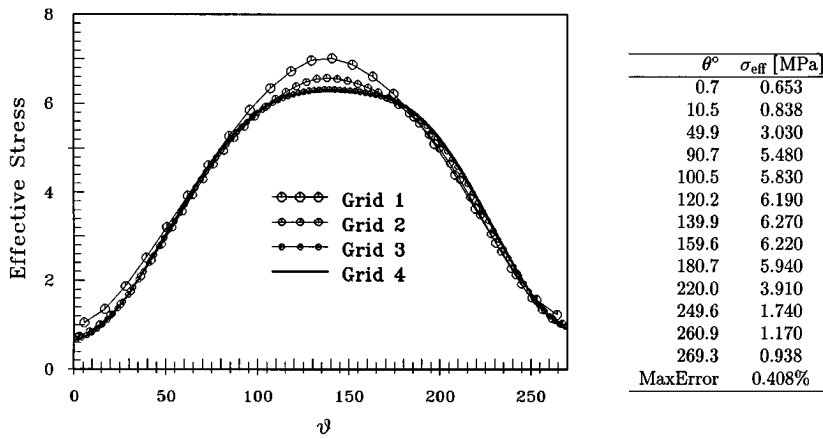


Figure 8. Distribution of effective stress at  $r = 1.5R, z = 0$  in case of T member

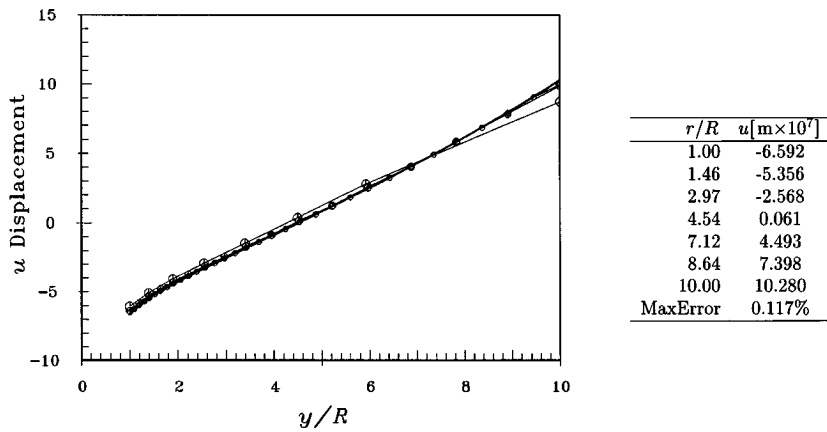
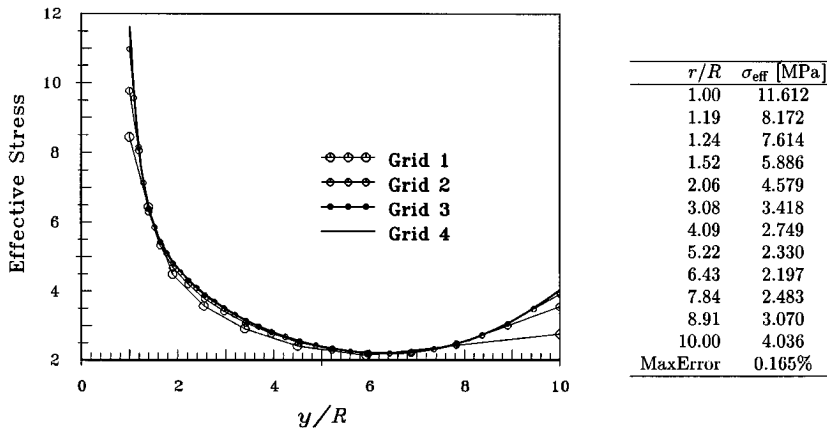


Figure 9. Distribution of effective stress (top) and  $u$  displacement component (bottom) along  $x = 0, z = 0$  for the case of T member

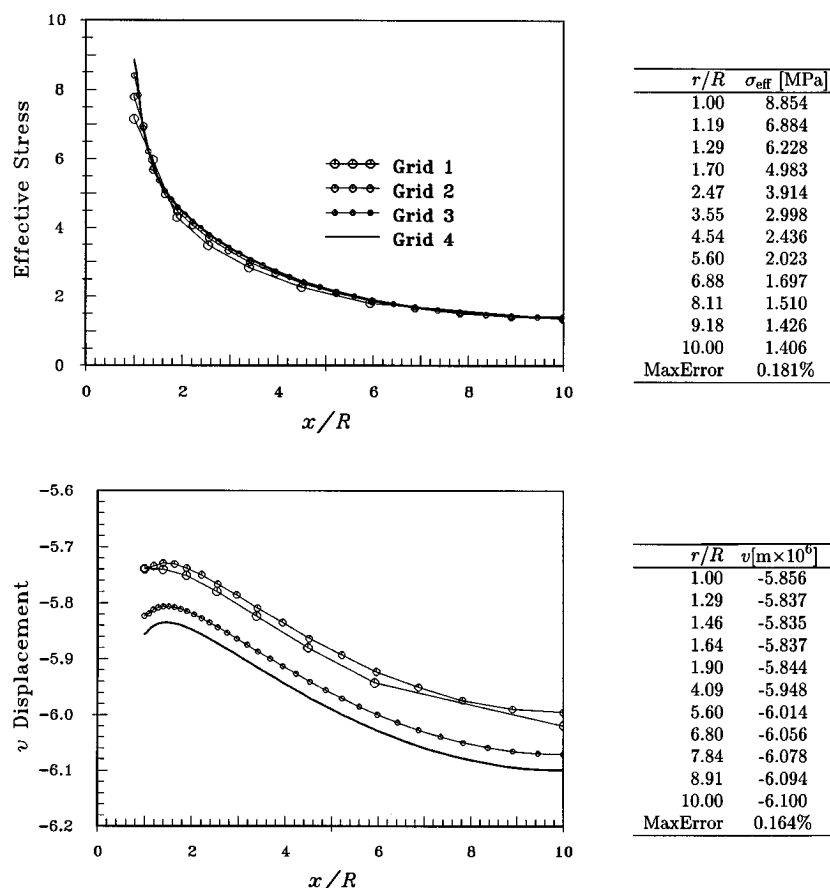


Figure 10. Distribution of effective stress (top) and  $v$  displacement component (bottom) along  $y = 0$ ,  $z = 0$  for the case of T member

are chosen for presentation. The profile along  $r = 1.5R$ ,  $z = 0$  is shown in Figure 8. The meanings of  $r$  and  $\theta$  co-ordinates are explained in Figure 5. Results for all four grids are shown, indicating rapid convergence towards a grid-independent solution. The profiles are almost symmetric with respect to the location  $\theta = 135^\circ$ , where the maximum value of the effective stress occurs. The maximum is not very much pronounced but is rather flat, spanning over almost  $60^\circ$ . The minimum values are at the non-loaded boundaries, corresponding to  $\theta = 0^\circ$  and  $\theta = 270^\circ$ . The key points along the profile on the finest grid are given in the table on the right-hand side of Figure 8. The maximum error in the solution on the finest grid, estimated using Richardson extrapolation, is also indicated.

The profiles of the effective stress and  $u$  and  $v$  displacement components in the  $z = 0$  plane along directions  $x = 0$  and  $y = 0$ , respectively, are shown in Figures 9 and 10. The effective stress rises sharply towards the edge of the circular hole indicating large stress concentration there. The profile in plane  $x = 0$  has a local minimum at  $y = 6.4R$ . The  $u$  displacement component in this plane changes sign at  $y = 4.7R$ , indicating that the upper part of the flange is stretched and the lower one compressed in the  $x$  direction. The variation is almost linear between the minimum  $u_{\min} = -6.59 \times 10^{-7}$  m and the maximum  $u_{\max} = 1.028 \times 10^{-6}$  m at the hole edge and upper boundary, respectively.

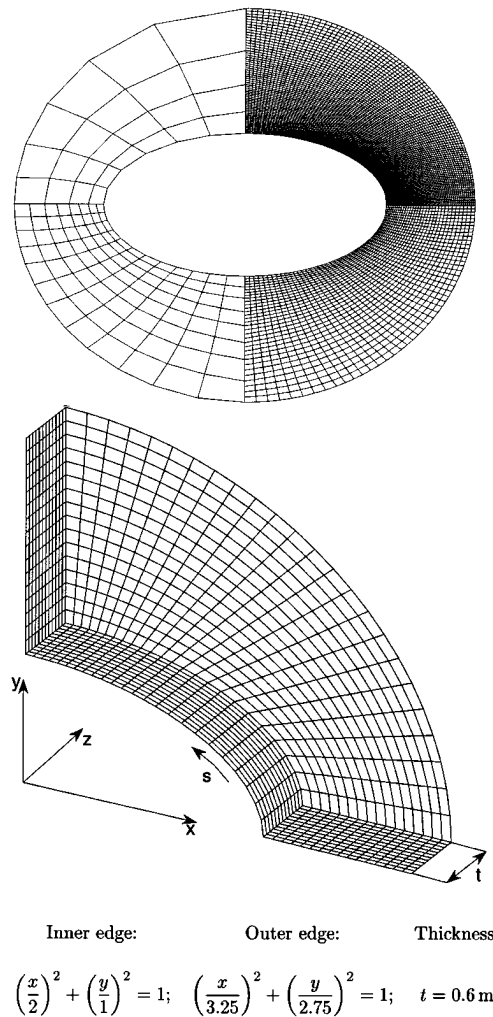


Figure 11. Numerical grids used for prediction of a thick plate bending

The  $v$  displacement component along  $y = 0, z = 0$  varies non-linearly, as shown in Figure 10. Here a non-monotonic convergence towards a grid-independent solution is observed. There is a small increase in  $v$  after the first refinement, and thereafter the values are reducing. Note that the scale has been largely stretched to show this behaviour.

The maximum error on the finest grid for all quantities is estimated to be less than 0.5 per cent. Average errors in profiles presented in Figures 8, 9 and 10 are of the order of 0.1 per cent. These results are therefore suitable for testing the accuracy of solution methods.

#### 4.3. Bending of a thick plate

A thick elliptic plate with a centred elliptic hole, fully clamped at the outside edge and loaded by a constant pressure of 1 MPa at the upper surface, was proposed as a test case by

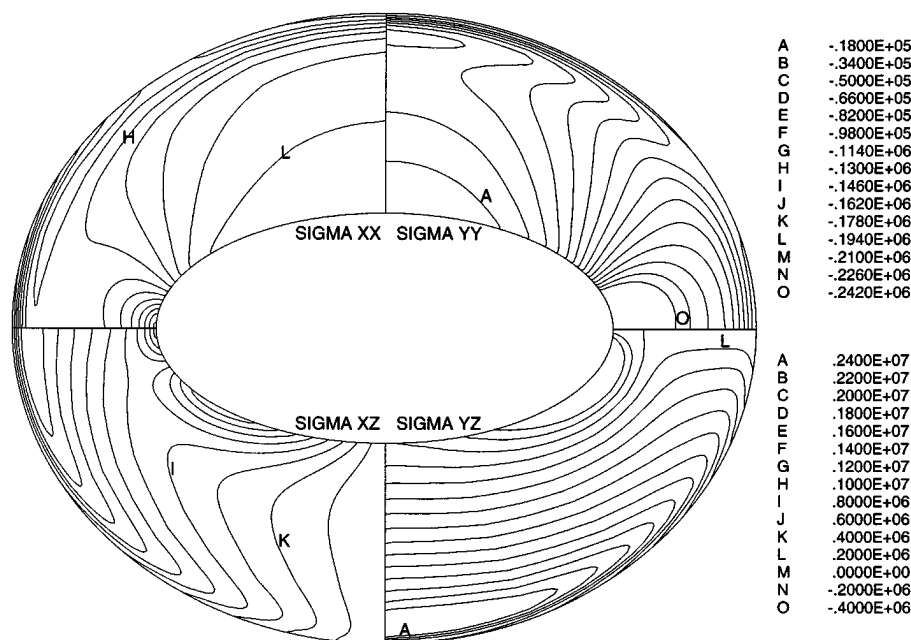


Figure 12. Distribution of  $\sigma_{xx}$ ,  $\sigma_{yy}$ ,  $\sigma_{xz}$  and  $\sigma_{yz}$  in plane  $z = 0.3$  m (The legend in the upper part refers to the distribution of  $\sigma_{xx}$  and  $\sigma_{yy}$ , and in the lower part to the distribution of  $\sigma_{xz}$  and  $\sigma_{yz}$ )

NAFEMS (National Agency for Finite Element Methods and Structures). The out-of-plate bending is the key feature of interest. Due to a double symmetry, only a quarter of the plate is analysed.

Calculations were performed on five systematically refined grids ranging between 72 and 294 912 CVs. The grids are shown in Figure 11 together with the co-ordinate system adopted, with respect to which the results are presented. The distribution of stress tensor components in plane  $z = 0.3$  m are plotted in Figure 12. The  $\sigma_{zz}$  component in this plane is almost constant (approximately  $-0.55$  MPa).

The symmetry between  $\sigma_{xx}$  and  $\sigma_{yy}$ , and  $\sigma_{xz}$  and  $\sigma_{yz}$  stress components across planes  $x = y$  and  $x = -y$ , which would be expected in the case of a circular plate with a circular hole, can be noticed in a distorted form. The largest distortion exists in the region where the radius of curvature of the inner ellipse is smallest. The stress components  $\sigma_{xz}$  and  $\sigma_{yz}$  are almost one order of magnitude larger than other components and in this plane they dominate the distribution of the effective stress.

Although in this case there is no local stress concentration as in the previous one, the stresses show strong variation in the whole domain and the variation is not monotonic.

In Figure 13 the distribution of the local stress component  $\sigma_{ss}$  along the local co-ordinate  $s$  is presented for different grids. The local co-ordinate  $s$  runs along the upper inner edge of the plate in the direction shown in Figure 11. This profile is the one proposed by NAFEMS for testing. It should be noted that there are no computational points along such edges in finite volume discretization, so the values of the stress tensor components used to calculate  $\sigma_{ss}$  are obtained by linearly extrapolating their values from the control volumes adjacent to the edge. In the case of a circular plate with a circular hole, the value of  $\sigma_{ss}$  would be constant, so the distortion of the profile that can be observed in Figure 13 is due to the change of curvature radius.

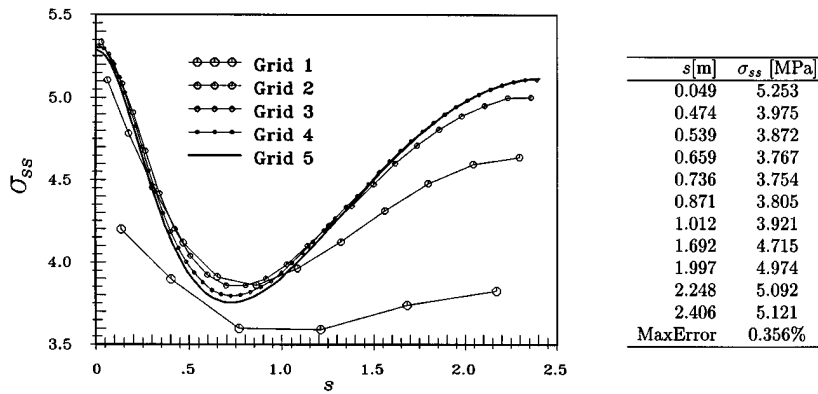


Figure 13. Distribution of local stress  $\sigma_{ss}$  along local co-ordinate  $s$  for the elliptic plate

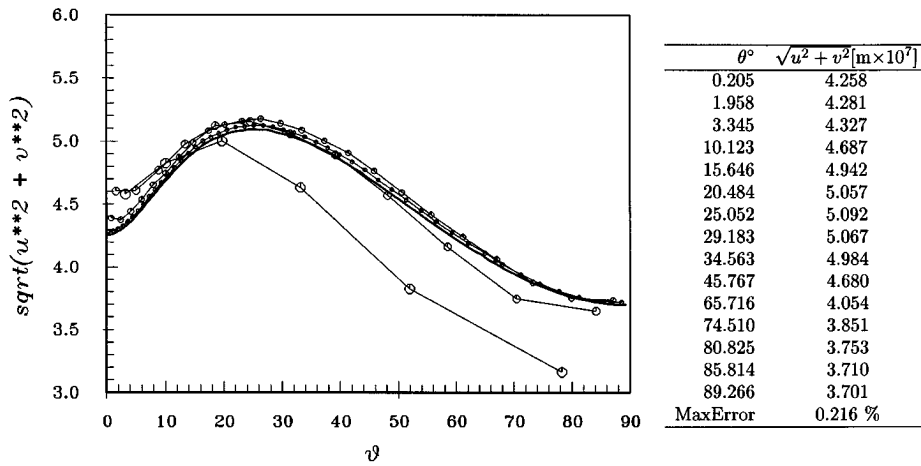
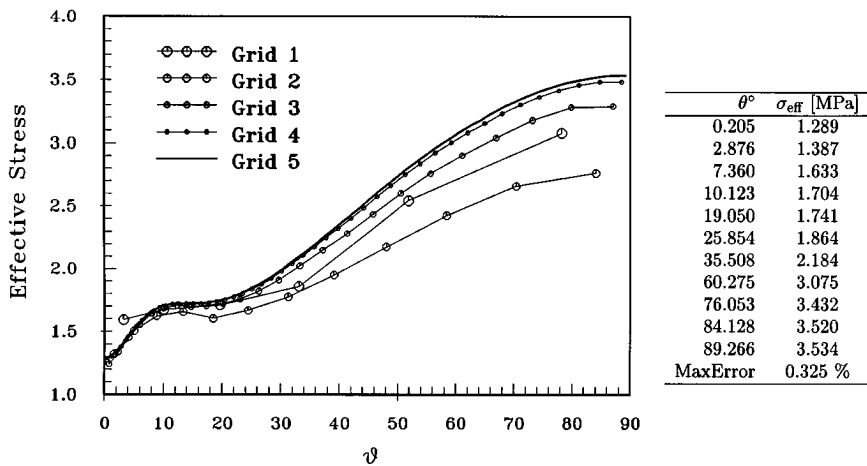


Figure 14. Distribution of effective stress (top) and the magnitude of displacement component (bottom) in  $x$ - $y$  plane along  $r = 2.1$  m,  $z = 0.3$  m for the elliptic plate

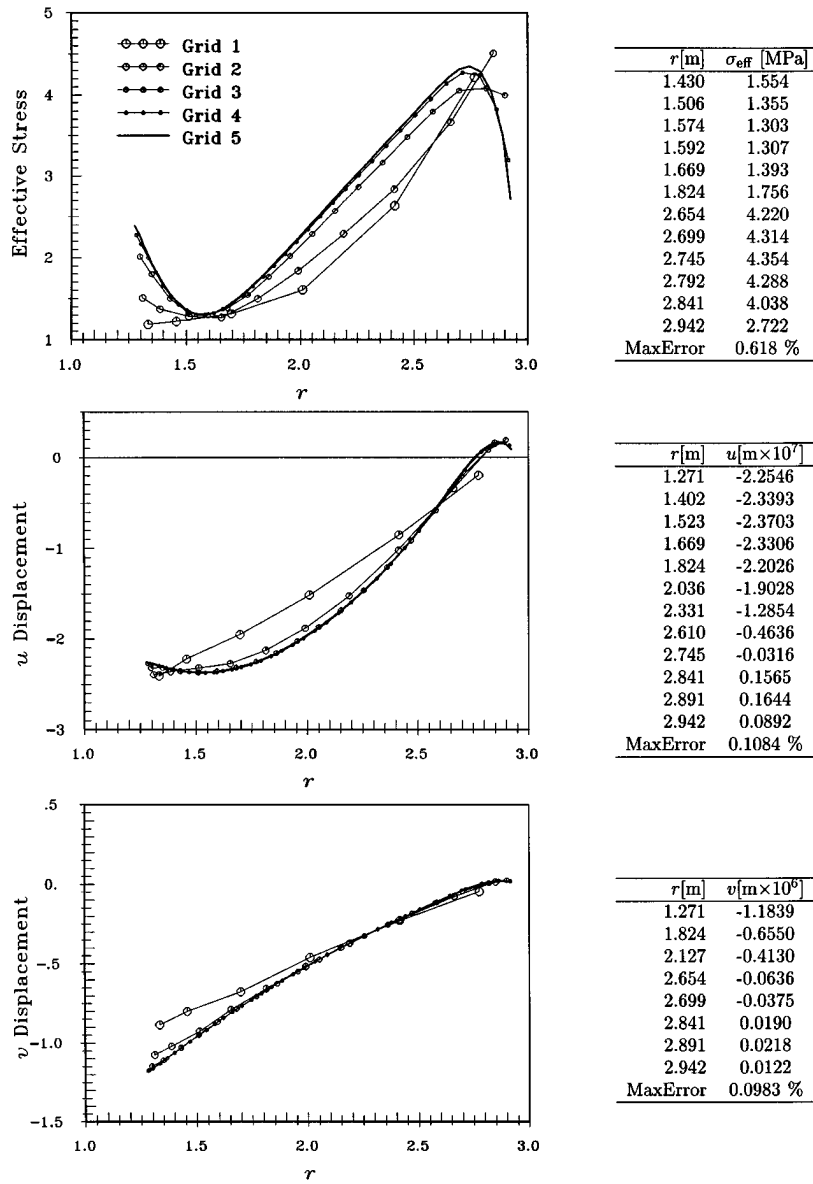


Figure 15. Distribution of effective stress (top) and displacement components  $u$  (middle) and  $v$  (bottom) along  $x = y$ ,  $z = 0.3$  m for the elliptic plate

The results show convergence towards the grid-independent solution as the grid is refined; however, the convergence is not monotonic everywhere. Since five grids were used, the difference between solutions on the two finest grids still allows for a reliable estimation of discretization errors. The average errors were in this case, as in the previous one, of the order of 0.1 per cent. The maximum error occurs in the region of the local minimum of  $\sigma_{ss}$  and is less than 0.4 per cent.

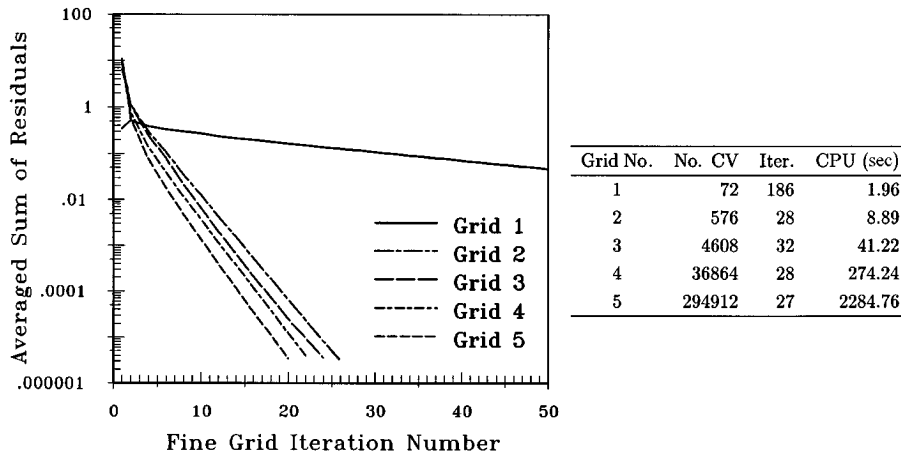


Figure 16. Convergence properties for the elliptic plate problem

Table II. Memory and CPU times necessary to obtain converged solution on all grid levels using double precision arithmetics on an IBM RISC System 6000/530 workstation

Case	No. CVs	No. deg. freedom	No. grid levels	Memory (MB)	Sol. Tol. = $10^{-5}$		Sol. Tol. = $10^{-3}$	
					Fine grid Iter.	CPU (min)	Fine grid Iter.	CPU (min)
1	12 288	24 576	6	8.85	12	1.3	6	0.7
2	319 488	958 464	4	161.66	66	106.9	32	51.4
3	294 912	884 736	5	148.19	27	38.1	16	22.6

The distribution of the effective stress  $\sigma_{ss}$  and displacement components  $u$  and  $v$  along  $r = \sqrt{x^2 + y^2} = 2.1$  m,  $z = 0.3$  m is shown in Figure 14. One can observe a steady increase of the effective stress with the increasing angle  $\theta$ . At approximately  $\theta = 15^\circ$  the profile has an inflection point. The profile of the displacement in the  $x$ - $y$  plane has a well-pronounced maximum at  $\theta = 25.05^\circ$  and its value is  $5.0918 \times 10^{-7}$  m.

Finally, the profiles of the effective stress and displacement component  $u$  and  $v$  along  $x = y$ ,  $z = 0.3$  m are presented in Figure 15. The effective stress profile has a very sharp minimum at  $r = 1.574$  m and maximum at  $r = 2.745$  m. These extreme values of the effective stress profile are mainly determined by the distribution of  $\sigma_{xz}$  and  $\sigma_{yz}$  stress components (see Figure 12).

In contrast to the result expected for a circular plate, where the profiles of  $u$  and  $v$  displacement components are the same along the specified direction, here a large difference can be observed between them. The maximum absolute value of the  $v$  displacement component along the profile is almost an order of magnitude larger than the maximum value of  $u$ . At the same time, the  $u$  displacement profile exhibits two extremes, one at  $r = 1.523$  m and the other at  $r = 2.891$  m. Both displacement components change sign,  $u$  at  $r = 2.760$  m and  $v$  at  $2.772$  m.

In all of the above profiles, convergence towards a grid-independent solution, although non-monotonic over the range of grids used, is clearly seen. The error in the solution on the finest grid is on average about 0.1 per cent. Maximum errors are indicated for each profile in Figures 13–15.

Figure 16 shows the asymptotic convergence rate of the full multigrid solution method for the set of numerical grids used in this case. The number of fine grid iterations is almost constant and the CPU time is proportional to the number of computational points.

## 5. CONCLUSIONS

Three benchmark cases were proposed for assessing the accuracy and efficiency of numerical methods for structural analysis. The paper provides accurate, grid-independent solutions in the form of graphs as well as tables containing the values at key points on the profiles.

The solutions were obtained by using a succession of uniformly refined grids and the discretization errors were estimated using Richardson extrapolation. For all results presented, the maximum estimated error is found to be less than 0.7 per cent, while the average error is about 0.1 per cent.

The convergence tolerance for all cases presented was  $10^{-5}$ , which corresponds to the accuracy to within four to five significant figures. However, for most practical applications discretization errors of the order of 1 per cent are acceptable and the convergence tolerance of  $10^{-3}$  would suffice; the number of required iterations and computing time are much lower in this case.

The use of multigrid acceleration resulted in respectable computing times, while segregated solution algorithm imposed very small memory demands. Memory and CPU times necessary to perform double-precision calculations on an IBM RISC System 6000/530 workstation, for all three test cases, are given in Table II.

## REFERENCES

1. I. Demirdžić and S. Muzaferiya, 'Finite volume method for stress analysis in complex domains', *Int. j. numer. methods eng.*, **37**, 3751–3766 (1994).
2. I. Demirdžić and S. Muzaferiya, 'Numerical method for coupled fluid flow, heat transfer and stress analysis using unstructured moving meshes with cells of arbitrary topology', *Comput. Methods Appl. Mech. Eng.*, **125**, 235–255 (1995).
3. M. Hortman, M. Perić and G. Scheuerer, 'Finite volume multigrid prediction of laminar natural convection: bench-mark solutions', *Int. j. numer. methods fluids*, **11**, 189–207 (1990).
4. H. A. van der Vorst and P. Sonneveld, 'CGSTAB: A more smoothly converging variant of CG-S', *Technical Report 90-50*, Delft University of Technology, 1990.
5. J. A. Meijerink and H. A. van der Vorst, 'Guidelines for the usage of incomplete decompositions in solving sets of linear equations as they occur in practical problems', *J. Comput. Phys.*, **44**, 134–155 (1981).
6. A. Brandt, 'Multi-level adaptive solutions to boundary-value problems', *Math. Comput.*, **31**, 333–390 (1977).
7. S. P. Timoshenko and J. N. Goodier, *Theory of Elasticity*, 3rd edn, McGraw-Hill, London, 1970.
8. O. C. Zienkiewicz and J. Z. Zhu, 'The superconvergent patch recovery and a posteriori error estimates. Part 1: The recovery technique', *Int. j. numer. methods eng.*, **33**, 1331–1364 (1992).
9. A. Ivanković, I. Demirdžić, J. G. Williams and P. S. Leever, 'Application of the finite volume method to the analysis of dynamic fracture problems', *Int. J. Fracture*, **66**, 357–371 (1994).